

Creation of a Chiral Bobber Lattice in Helimagnet-Multilayer Heterostructures

Kejing Ran,^{1,2,*} Yizhou Liu,^{3,*} Yao Guang,⁴ David M. Burn,⁵ Gerrit van der Laan,^{5,†} Thorsten Hesjedal,^{6,‡} Haifeng Du,^{7,§} Guoqiang Yu,^{4,||} and Shilei Zhang^{1,2,¶}¹School of Physical Science and Technology, ShanghaiTech University, Shanghai 200031, China²ShanghaiTech Laboratory for Topological Physics, ShanghaiTech University, Shanghai 200031, China³RIKEN Center for Emergent Matter Science (CEMS), Wako 351-0198, Japan⁴Beijing National Laboratory for Condensed Matter Physics, Institute of Physics, Chinese Academy of Sciences, Beijing 100190, China⁵Diamond Light Source, Harwell Science and Innovation Campus, Didcot, Oxfordshire OX11 0DE, United Kingdom⁶Clarendon Laboratory, Department of Physics, University of Oxford, Parks Road, Oxford OX1 3PU, United Kingdom⁷The Anhui Key Laboratory of Condensed Matter Physics at Extreme Conditions, High Magnetic Field Laboratory and University of Science and Technology of China, Chinese Academy of Science (CAS), Hefei, Anhui 230031, China

(Received 31 July 2020; revised 26 October 2020; accepted 20 November 2020; published 8 January 2021)

A chiral bobber is a localized three-dimensional magnetization configuration, terminated by a singularity. Chiral bobbers coexist with magnetic skyrmions in chiral magnets, lending themselves to new types of skyrmion-complementary bits of information. However, the on-demand creation of bobbers, as well as their direct observation remained elusive. Here, we introduce a new mechanism for creating a stable chiral bobber lattice state via the proximity of two skyrmion species with comparable size. This effect is experimentally demonstrated in a $\text{Cu}_2\text{OSeO}_3/[\text{Ta}/\text{CoFeB}/\text{MgO}]_4$ heterostructure in which an exotic bobber lattice state emerges in the phase diagram of Cu_2OSeO_3 . To unambiguously reveal the existence of the chiral bobber lattice state, we have developed a novel characterization technique, magnetic truncation rod analysis, which is based on resonant elastic x-ray scattering.

DOI: 10.1103/PhysRevLett.126.017204

Magnetic skyrmions are two-dimensional, particlelike solitonic field configurations with extraordinary topological properties [1,2]. Although most magnetic systems in which skyrmions exist are essentially three-dimensional (3D) objects, the skyrmion is classified by elements of the homotopy group $\pi_2(S^2)$ [3]. Recently, complex 3D magnetic textures were found, which are classified by the $\pi_3(S^2)$ group [4–19], providing an ideal playground for studying topological defects and magnetic monopole-related science. Therefore, the experimental exploration of 3D magnetic structures with topological properties has become an important task.

A major class of materials that hosts 3D skyrmion structures are chiral magnets, such as MnSi [20], FeCoSi [21], FeGe [22], Cu_2OSeO_3 [23], CoZnMn [24], and so on. In these bulk materials (with periodic boundary condition), a particular energy hierarchy leads to the formation of multidimensional solitons: $w = A(\nabla\mathbf{m}^2) + D\mathbf{m} \cdot (\nabla \times \mathbf{m}) - \mathbf{B} \cdot \mathbf{m} + w_D$, where $\mathbf{m}(x, y, z)$ is the real-space magnetization configuration. The energy density w

contains first three local terms, i.e., exchange interaction with stiffness constant A , Dzyaloshinskii-Moriya interaction (DMI) with a strength of D , a Zeeman term that scales with external field \mathbf{B} , and a nonlocal dipole-dipole interaction term w_D . The system is thus described by a modulated structure, with characteristic periodicity $\lambda_h = 4\pi A/D$. It was recognized that under certain perturbations, such as magnetocrystalline anisotropy or thermal fluctuations, a skyrmion lattice state can form in a narrow region of the temperature-magnetic field phase diagram between the lower and upper critical fields, B_{A1} and B_{A2} , respectively, close to the transition temperature, although the lowest energy ground state is the one-dimensional modulated conical state [2,20,25–27]. Under these conditions, the 2D skyrmion lattices are stacked along the field direction, forming the skyrmion tube lattice (SkTL) structure.

For chiral magnets with a finite thickness that is comparable to λ_h , the terminating surfaces break translational symmetry, leading to a surface twist effect [4,6,10,28]. Surface twisting is responsible for a number of phenomena: (i) a modulation of the 3D skyrmion tubes along the field direction (with varying helicity angle) [6,10,29], and, consequently, (ii) an enhanced energetic stability over the conical phase, witnessed by the largely expanded skyrmion region in the phase diagrams [6,22].

Published by the American Physical Society under the terms of the Creative Commons Attribution 4.0 International license. Further distribution of this work must maintain attribution to the author(s) and the published article's title, journal citation, and DOI.

(iii) At higher fields above B_{A2} , a metastable surface state, i.e., the chiral bobbers (ChBs), which represent a new type of 3D topological texture, can be generated through a nonequilibrium process [5,13].

Chiral bobbers are characterized by a distinct 3D structure, resembling a floating bobber, that consists of a skyrmion stack with continuously reducing diameter away from the surface with a bobber length L_p , eventually shrinking down to a singularity, the Bloch point (BP) [5]. Such a topological point defect has finite energy, revealing itself as a metastable state at fields larger than B_{A2} , where the conical phase dominates [5,13]. The study of ChBs is of great interest due to the presence of the BP, which resembles a monopole structure with emergent dynamical behavior [16,18,30,31]. Therefore, the ChB phase provides an excellent platform for the general study of topological defect-related physics. Moreover, due to the similar energy barriers between ChBs and SkTs, bobbers can serve as promising information carriers for advanced memory devices in conjunction with skyrmions, where the presence of either represents a different information state [13,32].

Nevertheless, the creation of bobbers has been a challenging task. So far, the mechanism that stabilizes ChBs largely relies on their metastable nature, i.e., they can be produced by either field-cooling or field-tilting protocols [13]. In both scenarios, bobbers seem to randomly nucleate at arbitrary positions within the surface [13]. This prevents further experimental studies of their novel properties, and hinders their use in future racetrack memory. Recent work hints at the possibility that the exotic interface Rashba DMI can stabilize ChBs in epitaxially grown FeGe thin films [15], however, the unambiguous experimental characterization of the bobber structure, including their shape and penetration length, still remains elusive. In this Letter, we present a new mechanism to create ChBs in a controlled manner, as well as a new experimental technique for their direct observation.

Figure 1(a) shows the key concept of the new mechanism that we adopted to stabilize the chiral bobber lattice (ChBL) in a heterostructure formed by a bulk Cu_2OSeO_3 crystal and a multilayered (ML) thin film. Cu_2OSeO_3 is a well-known SkTL-hosting chiral magnet, which has a helical wavelength $\lambda_h \approx 56$ nm, a transition temperature $T_C \approx 57$ K, and an upper critical field $B_{A2} \approx 37$ mT [33]. Using resonant elastic x-ray scattering (REXS), it was shown that surface twisting is a pronounced effect at the Cu_2OSeO_3 [001] surface. Nevertheless, a bobber phase has not been observed in chiral bulk magnets [10,33]. Our strategy for obtaining bobbers is to make use of proximity coupling between two skyrmion systems with comparable lateral dimensions. In the case of Cu_2OSeO_3 bulk crystals, we selected a tunable $[\text{Ta}/\text{CoFeB}/\text{MgO}]_n$ multilayer structure. In an earlier study, we have shown that skyrmions with diameters of ~ 100 nm can be stabilized in such ML

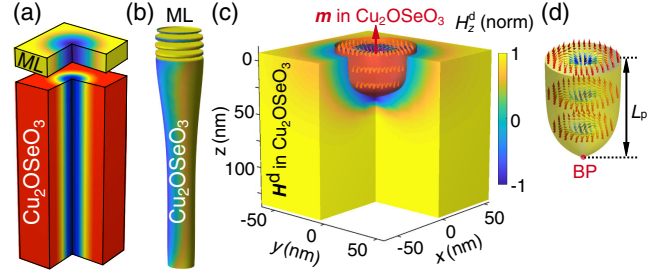


FIG. 1. Creation of a chiral bobber structure via heterostructure engineering. (a) Illustration of the heterostructure by contacting two different skyrmion species with comparable lateral dimensions. (b) Simulation results of the skyrmion tube structure at field between B_{A1} and B_{A2} . (c) z component of the dipolar field distribution from a skyrmion in the multilayer. (d) Calculated chiral bobber structure formed in Cu_2OSeO_3 at a field between the first and second upper critical fields B_{A2} and B_{A3} , respectively.

systems in a relatively broad range of magnetic fields and temperatures, covering the range of B_{A1} to B_{A2} of Cu_2OSeO_3 [34]. Consequently, two interactions will be dominating the heterostructure. First, the interface between Cu_2OSeO_3 and CoFeB can be mediated by a thin Ta layer, supporting a Ruderman-Kittel-Kasuya-Yosida (RKKY)-like exchange interaction J_{RKKY} across the two interface layers.

Such an interfacial exchange locks the positions of the skyrmions in the ML, and aligns them with the bulk skyrmions, as shown by our micromagnetic simulations using MuMax3 in Fig. 1(b) [35]. The interfacial exchange effect connects the two SkT species, and accommodates their difference in lateral dimension by forming a smoothly varying 3D funnel-like structure. Second, due to the larger saturation magnetization M_S in the ML, the dipole-dipole interaction leads to a relatively strong nonlocal stray field, influencing the SkTs in the bulk crystal.

Figure 1(c) shows the calculated distribution of the z component of the dipolar field H_z^d in the bulk region. The shape of the stray field and the energy density w_D resembles that of a bobberlike structure. For the field range of $B_{A1} < B < B_{A2}$, the intrinsic interactions coming from bulk Cu_2OSeO_3 dominate over the dipolar interaction from the multilayer, forming a standard SkTL phase—unaffected by interfacial effects. At fields slightly above B_{A2} , however, the SkTL state in Cu_2OSeO_3 starts to evolve into the conical phase, following a first-order type phase transition [36]. Nevertheless, the skyrmion state in the ML remains intact, taking on a funnel-like structure in the near-surface region of Cu_2OSeO_3 . Subsequently, the ML skyrmion dipolar field [Fig. 1(c)] breaks the SkTL in the bulk, leading to the formation of bobbers with a finite depth L_p , as shown in Fig. 1(d).

The $[\text{Ta}/\text{CoFeB}/\text{MgO}]_4$ multilayer structure was grown by magnetron sputtering on a finely polished Cu_2OSeO_3 [001] substrate, following the recipe in Ref. [34]. The inset

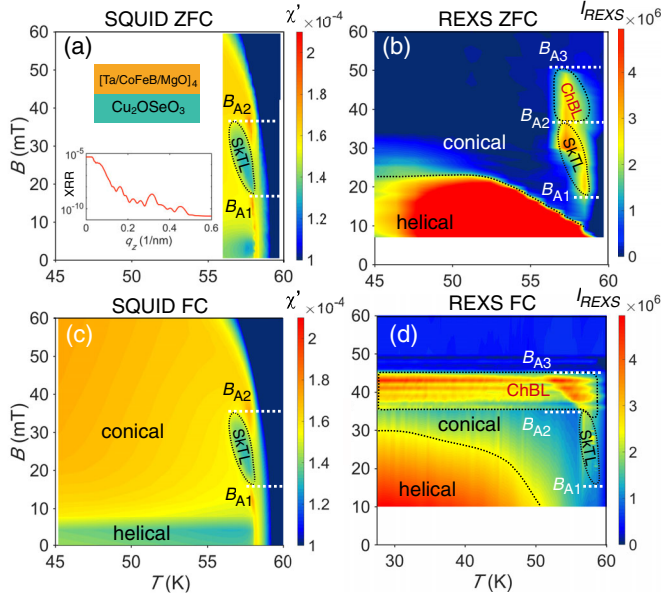


FIG. 2. Phase diagrams mapped by (a),(c) ac susceptibility and (b),(d) REXS on the same ML/Cu₂SeO₃ sample. (a),(b) Measurements carried out after zero-field cooling and (c),(d) after field cooling. The lower critical field B_{A1} and the upper critical field B_{A2} enclose the SkTL pocket, whereas the ChBL state reached from B_{A2} to the second upper critical field B_{A3} .

in Fig. 2(a) shows the x-ray reflectivity (XRR) profile, characterized by a smoothly decaying specular intensity with superimposed fringes, suggesting a well-defined heterostructure interface and excellent superstructure film quality. Next, the magnetic phase diagram of the *same* heterostructure sample was mapped out using two complementary techniques: (i) The ac susceptibility, measured in a superconducting quantum interference device (SQUID) magnetometer, is dominated by the Cu₂OSeO₃ *bulk* properties. (ii) REXS in reflection geometry, with the photon energy tuned to the Cu L_3 edge, measures the *surface* properties of Cu₂OSeO₃ only, down to a depth of < 100 nm [29].

Figure 2(a) and 2(b) show the phase diagrams mapped by ac susceptibility and REXS for $\mathbf{B} \parallel [001]$ and using zero-field cooling. The system exhibits the typical phase diagrams for skyrmion-hosting chiral magnets, as shown in Fig. 2(a), from which the SkTL phase can be clearly singled out near T_C . The lower and upper critical field values of B_{A1} and B_{A2} are consistent with other reports on Cu₂OSeO₃ [33]. On the other hand, REXS is able to unambiguously confirm the SkTL phase with its characteristic sixfold-symmetric diffraction pattern [33,37,38]. As shown in Fig. 2(b), we surprisingly find an additional phase pocket, located above the critical field B_{A2} . This phase again shows a sixfold-symmetric REXS pattern, identical to the one of the SkTL lattice [39]. The pattern even survives in fields above 50 mT (at 57 K), nevertheless, this phase is invisible to bulk-sensitive SQUID measurements. It is worth noting

that throughout our REXS experiments, the photon energy was tuned to the Cu L_3 edge (931.25 eV), which exclusively probes the surface region of Cu₂OSeO₃ [41]. We thus ascribe the origin of the phase pocket region from B_{A2} to the second upper critical field B_{A3} to the interfacial effect from the multilayer [labeled chiral bobber lattice (ChBL) state in the figure for reasons that will soon become clear].

Figures 2(c) and 2(d) show the phase diagrams after field-cooling from above T_C . It is recognized that a metastable skyrmion phase can be observed at temperatures far below T_C , which is obtained by field cooling as well [30], however, which reveals itself in *bulk* ac susceptibility measurement [42]. In our case, no metastable skyrmion state was in the SQUID measurements shown in Fig. 2(c). Instead, the phase diagram is almost identical to the one shown in Fig. 2(a). The standard SkTL phase, which exists between B_{A1} and B_{A2} , can also be easily singled out in REXS measurements as shown in Fig. 2(d). More interestingly, the ChBL phase is developing metastable behavior when cooling down the system, while the critical field values of B_{A2} and B_{A3} remain roughly consistent with those obtained from Fig. 2(b). This additional high-field phase, and its metastable behavior, provides strong clues hinting at the possible existence of chiral bobbers.

In order to fully characterize the magnetic structure of the ChBL phase, we developed magnetic truncation rod (MTR) analysis, a new REXS-based characterization technique. In general, crystalline truncation rods occur in many surface diffraction processes in which the incidence waves (e.g., x rays or electrons) are sensitive to the terminating surface of a crystal, either due to a small incident angle or shallow probing depth [43]. In such a scenario, delta-function-like diffraction peaks in reciprocal space are extending into rods in the direction of the surface normal. By analyzing the rod profile, one is able to “reconstruct” the detailed near-surface structure, which is especially useful when the structure shows a depth dependence [43].

Here, we extend the crystalline truncation rod theory to magnetic structures probed by soft x-ray resonant magnetic diffraction [39]. The SkTL phase in Cu₂OSeO₃ can be regarded as long-range-ordered magnetic crystal, shown in Fig. 3(a). The hexagonal unit cell has a (magnetic) lattice constant of $a = 65$ nm, with the motif being a single skyrmion. Such a two-dimensional skyrmion crystal is associated with the reciprocal space pattern shown in Fig. 3(b) with six 2D lattice peaks, i.e., (10), (11), (01), ($\bar{1}0$), ($\bar{1}\bar{1}$), and (0 $\bar{1}$). The origin is at the Γ point and the reciprocal lattice constant is $a^* = 4\pi/\sqrt{3}a$. Likewise, the magnetic Miller indices (H, K, L) can be defined in terms of magnetic reciprocal lattice units (m.r.l.u.). For soft x rays at resonance (with the Cu L_3 edge in this case), the penetration length Λ is usually below 100 nm [41], suggesting a pronounced effect of surface magnetic diffraction. Consequently, the six peaks are extended into rods along L , i.e., *magnetic*

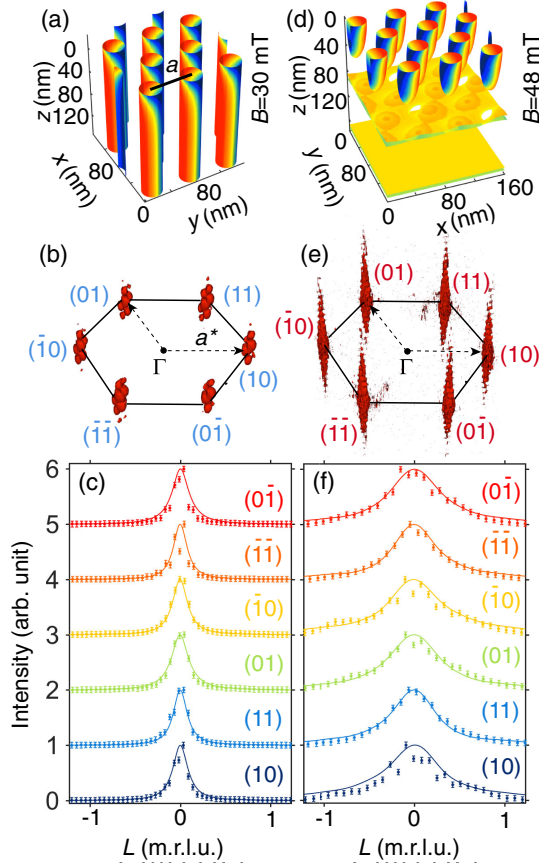


FIG. 3. Magnetic truncation rod analysis of skyrmions and chiral bobbers. (a) Micromagnetic simulation results of the SkTL phase. The colors of the $m_z = 0$ isosurface illustrate the local m_x and m_y in-plane magnetization components. (b) REXS intensity distribution in 3D reciprocal space, measured in the SkTL state at 57 K and 30 mT. (c) MTR profiles for six rods in the SkTL state as indicated. Circles represent experimental data (with error bars), and solid lines are fitted truncation rods using the simulated magnetic structure shown in (a). (d)–(f) Corresponding micromagnetic simulation results, REXS pattern, and MTR profiles for the chiral bobber lattice measured at 57 K and 48 mT.

truncation rods. They are thus expressed by a structure factor of the form $\mathbf{F}(\mathbf{q}) = -\hat{M}[iF^{(1)}(\mathbf{e}_s^* \times \mathbf{e}_i) \cdot \hat{\mathbf{n}}]$, where \mathbf{q} is the elastic scattering momentum transfer, which has to equate a reciprocal lattice vector (H, K, L) (of the magnetic lattice) to satisfy the diffraction condition. $F^{(1)}$ relates to the energy dependent dipole-transition amplitude of the magnetic scattering, \mathbf{e}_s and \mathbf{e}_i denote the unit vectors of the scattered and incident x-ray polarization, and $\hat{\mathbf{n}} = (n_1, n_2, n_3)$ is the unit vector of the local magnetic moment.

The quantity \hat{M} in the structure factor $\mathbf{F}(\mathbf{q})$ can be expressed as

$$\hat{M} = \frac{1}{\Lambda} \sum_{z=0}^{\infty} e^{-2z \sec \alpha / \Lambda} \sum_n e^{2\pi i \mathbf{q} \cdot \mathbf{r}_n}, \quad (1)$$

where $z = 0$ corresponds to the top surface, α is the incident angle, and the summation is carried out over all atomic positions n in the plane. For the photon energy tuned to the Cu L_3 edge, the x-ray attenuation length $\Lambda = 93.9$ nm [29]. Equation (1) allows us to calculate the MTRs in a layer-by-layer fashion. For ϵ_s summed over both polarizations, the MTR intensity $I(\mathbf{q}) = |\mathbf{F}(\mathbf{q})|^2$ [38] can be written as $I(\mathbf{q}) = \text{tr}[\hat{M} f_m u_i \hat{M} f_m^\dagger]$ (for details see Supplemental Material [39]).

Figure 3(b) shows the MTR data for $\text{Cu}_2\text{OSeO}_3/[\text{Ta}/\text{CoFeB}/\text{MgO}]_4$ measured in the SkTL phase at 57 K and 30 mT. The total intensity is the sum of the intensities measured with left- and right-circularly polarized incident light. The six magnetic Bragg peaks have a confined bloblike shape, which is slightly extended along the L direction. We ascribe this peak structure to the natural broadening owing to the finite penetration depth of soft x rays, reflecting the bulk character of 3D skyrmion tubes. The detailed rod profiles along L are shown in Fig. 3(c). The experimental data for the six rods can be almost perfectly reproduced in simulations of the MTRs based on the equation for $I(\mathbf{q})$ and using the micromagnetic simulation results shown in Fig. 3(a). It is worth mentioning that we also measured MTRs in the SkTL phase of a pristine Cu_2OSeO_3 [001] crystal (without a ML), which shows the same line shapes cutting through the rods along L .

Next, we measured MTRs in the bobber phase at 57 K and 48 mT. The 3D plot of the rod intensities is shown in Fig. 3(e). Although the ChBL state has the same reciprocal lattice in the H - K plane for $L = 0$, the rod profiles are significantly elongated along L —a signature of surface diffraction—with the x rays probing the shallow magnetization pattern buried right underneath the surface. Comparing the contrast in Figs. 3(b) and 3(e) suggests a very different depth profile of skyrmions and bobbers near the very interface of the heterostructure.

Figure 3(f) shows the MTR profiles of the six rods along L in the bobber phase. The peaks are significantly broadened compared to the skyrmion profiles shown in Fig. 3(c). By performing systematic numerical MTR simulations of micromagnetic models, we find that the contrast is sensitive to the 3D shape of the bobbers, as well as their extension in depth, L_p [39]. The six rods all have slightly different shapes as a result of a geometrical effect, i.e., as they are distributed at different azimuthal angles within the x - y plane, the x rays “see” them from a different perspective. Nevertheless, one should be able to fit all six rods at the same time using one 3D magnetic structure model. The solid lines in Fig. 3(f) are fitted rod profiles using the ChBL model obtained from micromagnetic simulations, shown in Fig. 3(d). The bobbers in Cu_2OSeO_3 form a well-ordered lattice with a bobber depth of $L_p = 40$ nm. The bobber shape, described by the skyrmion diameter evolution along z , can be extracted from our analysis. It is important to

point out that such precise L_p , as well as bobber shape with BP at the bottom are highly restricted by our numerical refinement, while other possible 3D near-surface structures can be excluded [39]. The experimental data agree well with our micromagnetic model, providing unambiguous evidence for the existence of a chiral bobber lattice.

It is worth mentioning that the rod broadening starts to take place just above B_{A2} , while we did not observe a gradual change of the peak width upon increasing the field. This indicates that the transition between SkTL and ChBL is accompanied by a sudden change of L_p . The value of ~ 40 nm is much larger than that of metastable bobbars in confined thin plate geometries, in which one can expect L_p to be smaller than $\lambda_h/2 = 28$ nm [5]. This difference in L_p values is due to the different stabilization mechanisms: whereas the bobber lattice state is stabilized via the interactions across the interface, geometrically confined geometry bobbars are due to the surface twist effect. Note that we also performed control experiments on $\text{Cu}_2\text{OSeO}_3/\text{Ta}$ and $\text{Cu}_2\text{OSeO}_3/\text{Pt}$ samples [39], which excludes possible contributions of Rashba spin-orbit coupling and induced surface anisotropy [44] to the formation of ChBL. Furthermore, everywhere within the ChBL phase between B_{A2} and B_{A3} , L_p maintains a value of (40 ± 5) nm. It is expected that by tuning the materials parameters of the ML, such as the CoFeB thickness and the repetition number n , L_p can be effectively engineered.

In summary, we uncovered a new mechanism for creating long-range-ordered chiral bobber lattices by coupling two skyrmion lattice states across a chiral bulk crystal-ferromagnetic heterostructure interface. Chiral bobbars are attractive topological structures, which remained elusive as their controlled stabilization was challenging. Our coupling approach unlocks a wide range of opportunities for the detailed study of the physical properties of bobbars, such as transport and dynamics. Further, magnetic truncation rod analysis in REXS is a powerful technique for studying skyrmions and bobbars, for determining complex 3D magnetic structures in general. The controlled nucleation of ChBs, which we have demonstrated here, is the prerequisite for their use in skyrmion-bobber memory [13,32].

The REXS experiments were carried out on beam line I10 at the Diamond Light Source, U.K., under proposal SI20182. The authors thank the Analytical Instrumentation Center (SPST-AIC10112914), School of Physical Science and Technology (SPST), ShanghaiTech University for SQUID and XRD characterizations. S. L. Z. acknowledges the starting grant from ShanghaiTech University and the National Key Research and Development Program of China (Grant No. 2020YFA0309400). K. J. R. acknowledges the support of the Shanghai Sailing Program (Grant No. 20YF1430600). G. Q. Y. thanks the National Natural Science Foundation of China (NSFC, Grant No. 11874409) and the Beijing Natural Science Foundation (Grant

No. Z190009) for their financial support. T. H. acknowledges support from the Engineering and Physical Sciences Research Council (UK) through Grant No. EP/N032128/1.

*These authors contributed equally to this work.

[†]Gerrit.vanderLaan@diamond.ac.uk

[‡]Thorsten.Hesjedal@physics.ox.ac.uk

[§]duhf@hmfl.ac.cn

^{||}guoqianguy@iphy.ac.cn

[¶]zhangshl1@shanghaitech.edu.cn

- [1] A. N. Bogdanov and D. A. Yablonskii, *Sov. Phys. JETP* **68**, 101 (1989) [*ZhETF* **95**, 178 (1989)], <http://www.jetp.ac.ru/cgi-bin/e/index/e/68/1/p101?a=list>.
- [2] N. Nagaosa and Y. Tokura, *Nat. Nanotechnol.* **8**, 899 (2013).
- [3] N. D. Mermin, *Rev. Mod. Phys.* **51**, 591 (1979).
- [4] F. N. Rybakov, A. B. Borisov, and A. N. Bogdanov, *Phys. Rev. B* **87**, 094424 (2013).
- [5] F. N. Rybakov, A. B. Borisov, S. Blügel, and N. S. Kiselev, *Phys. Rev. Lett.* **115**, 117201 (2015).
- [6] A. O. Leonov, Y. Togawa, T. L. Monchesky, A. N. Bogdanov, J. Kishine, Y. Kousaka, M. Miyagawa, T. Koyama, J. Akimitsu, T. Koyama, K. Harada, S. Mori, D. McGrouther, R. Lamb, M. Krajnak, S. McVitie, R. L. Stamps, and K. Inoue, *Phys. Rev. Lett.* **117**, 087202 (2016).
- [7] P. J. Ackerman and I. I. Smalyukh, *Nat. Mater.* **16**, 426 (2017).
- [8] A. O. Leonov, J. C. Loudon, and A. N. Bogdanov, *Appl. Phys. Lett.* **109**, 172404 (2016).
- [9] A. O. Leonov, T. L. Monchesky, J. C. Loudon, and A. N. Bogdanov, *J. Phys. Condens. Matter* **28**, 35LT01 (2016).
- [10] S. L. Zhang, G. van der Laan, W. W. Wang, A. A. Haghighirad, and T. Hesjedal, *Phys. Rev. Lett.* **120**, 227202 (2018).
- [11] J. C. Loudon, A. O. Leonov, A. N. Bogdanov, M. C. Hatnean, and G. Balakrishnan, *Phys. Rev. B* **97**, 134403 (2018).
- [12] H. Du, X. Zhao, F. N. Rybakov, A. B. Borisov, S. Wang, J. Tang, C. Jin, C. Wang, W. Wei, N. S. Kiselev, Y. Zhang, R. Che, S. Blügel, and M. Tian, *Phys. Rev. Lett.* **120**, 197203 (2018).
- [13] F. Zheng, F. N. Rybakov, A. B. Borisov, D. Song, S. Wang, Z.-A. Li, H. Du, N. S. Kiselev, J. Caron, A. Kovács, M. Tian, Y. Zhang, S. Blügel, and R. E. Dunin-Borkowski, *Nat. Nanotechnol.* **13**, 451 (2018).
- [14] M. Charilaou, H.-B. Braun, and J. F. Löffler, *Phys. Rev. Lett.* **121**, 097202 (2018).
- [15] A. S. Ahmed, J. Rowland, B. D. Esser, S. R. Dunsiger, D. W. McComb, M. Randeria, and R. K. Kawakami, *Phys. Rev. Mater.* **2**, 041401 (2018).
- [16] A. O. Leonov and K. Inoue, *Phys. Rev. B* **98**, 054404 (2018).
- [17] Y. Liu, R. K. Lake, and J. Zang, *Phys. Rev. B* **98**, 174437 (2018).
- [18] G. P. Müller, F. N. Rybakov, H. Jónsson, S. Blügel, and N. S. Kiselev, *Phys. Rev. B* **101**, 184405 (2020).
- [19] P. Fischer, D. Sanz-Hernández, R. Streubel, and A. Fernández-Pacheco, *APL Mater.* **8**, 010701 (2020).
- [20] S. Mühlbauer, B. Binz, F. Jonietz, C. Pfleiderer, A. Rosch, A. Neubauer, R. Georgii, and P. Böni, *Science* **323**, 915 (2009).

- [21] X. Z. Yu, Y. Onose, N. Kanazawa, J. H. Park, J. H. Han, Y. Matsui, N. Nagaosa, and Y. Tokura, *Nature (London)* **465**, 901 (2010).
- [22] X. Z. Yu, N. Kanazawa, Y. Onose, K. Kimoto, W. Z. Zhang, S. Ishiwata, Y. Matsui, and Y. Tokura, *Nat. Mater.* **10**, 106 (2011).
- [23] S. Seki, X. Z. Yu, S. Ishiwata, and Y. Tokura, *Science* **336**, 198 (2012).
- [24] Y. Tokunaga, X. Z. Yu, J. S. White, H. M. Ronnow, D. Morikawa, Y. Taguchi, and Y. Tokura, *Nat. Commun.* **6**, 7638 (2015).
- [25] A. N. Bogdanov and A. Hubert, *J. Magn. Magn. Mater.* **138**, 255 (1994).
- [26] M. N. Wilson, A. B. Butenko, A. N. Bogdanov, and T. L. Monchesky, *Phys. Rev. B* **89**, 094411 (2014).
- [27] A. Chacon, L. Heinen, M. Halder, A. Bauer, W. Simeth, S. Mühlbauer, H. Berger, M. Garst, A. Rosch, and C. Pfleiderer, *Nat. Phys.* **14**, 936 (2018).
- [28] S. A. Meynell, M. N. Wilson, H. Fritzsche, A. N. Bogdanov, and T. L. Monchesky, *Phys. Rev. B* **90**, 014406 (2014).
- [29] S. L. Zhang, G. van der Laan, J. Müller, L. Heinen, M. Garst, A. Bauer, H. Berger, C. Pfleiderer, and T. Hesjedal, *Proc. Natl. Acad. Sci. U.S.A.* **115**, 6386 (2018).
- [30] P. Milde, D. Köhler, J. Seidel, L. M. Eng, A. Bauer, A. Chacon, J. Kindervater, S. Mühlbauer, C. Pfleiderer, S. Buhardt, C. Schütte, and A. Rosch, *Science* **340**, 1076 (2013).
- [31] J. Wild, T. N. G. Meier, S. Pöllath, M. Kronseider, A. Bauer, A. Chacon, M. Halder, M. Schowalter, A. Rosenauer, J. Zweck, J. Müller, A. Rosch, C. Pfleiderer, and C. H. Back, *Sci. Adv.* **3**, e1701704 (2017).
- [32] M. Redies, F. R. Lux, J. P. Hanke, P. M. Buhl, G. P. Müller, N. S. Kiselev, S. Blügel, and Y. Mokrousov, *Phys. Rev. B* **99**, 140407(R) (2019).
- [33] S. L. Zhang, A. Bauer, D. M. Burn, P. Milde, E. Neuber, L. M. Eng, H. Berger, C. Pfleiderer, G. van der Laan, and T. Hesjedal, *Nano Lett.* **16**, 3285 (2016).
- [34] W. Li, I. Bykova, S. L. Zhang, G. Yu, R. Tomasello, M. Carpentieri, Y. Liu, Y. Guang, J. Gräfe, M. Weigand, D. B. Burn, G. van der Laan, T. Hesjedal, Z. Yan, J. Feng, C. Wan, J. Wei, X. Wang, X. Zhang, H. Xu, C. Guo, H. Wei, G. Finocchio, X. Han, and G. Schütz, *Adv. Mater.* **31**, 1807683 (2019).
- [35] A. Vansteenkiste, J. Leliaert, M. Dvornik, M. Helsen, F. Garcia-Sanchez, and B. Van Waeyenberge, *AIP Adv.* **4**, 107133 (2014).
- [36] M. Janoschek, M. Garst, A. Bauer, P. Krautscheid, R. Georgii, P. Böni, and C. Pfleiderer, *Phys. Rev. B* **87**, 134407 (2013).
- [37] S. L. Zhang, A. Bauer, H. Berger, C. Pfleiderer, G. van der Laan, and T. Hesjedal, *Appl. Phys. Lett.* **109**, 192406 (2016).
- [38] S. L. Zhang, G. van der Laan, and T. Hesjedal, *Nat. Commun.* **8**, 14619 (2017).
- [39] See Supplemental Material at <http://link.aps.org/supplemental/10.1103/PhysRevLett.126.017204> for details of the magnetic truncation rod (MTR) analysis and several key conclusions, which includes Ref. [40].
- [40] S. L. Zhang, A. Bauer, H. Berger, C. Pfleiderer, G. van der Laan, and T. Hesjedal, *Phys. Rev. B* **93**, 214420 (2016).
- [41] G. van der Laan, *C. R. Physique* **9**, 570 (2008).
- [42] A. Bauer and C. Pfleiderer, *Phys. Rev. B* **85**, 214418 (2012).
- [43] I. K. Robinson, *Phys. Rev. B* **33**, 3830 (1986).
- [44] A. J. Lee, A. S. Ahmed, B. A. McCullian, S. Guo, M. Zhu, S. Yu, P. M. Woodward, J. Hwang, P. C. Hammel, and F. Yang, *Phys. Rev. Lett.* **124**, 257202 (2020).